Solidification sequences in stainless steel dissimilar alloy welds

H. K. D. H. Bhadeshia, S. A. David, and J. M. Vitek

A series of laser and gas tungsten arc welds traversing stainless steels of different chemical compositions has been studied, to elucidate the role of austenite or ferrite nucleation and cooling rate on solidification behaviour. It has been found that a steel with a high Cr_{EQ}/Ni_{EQ} ratio can be induced to solidify as metastable austenite by initiating the weld in a steel with a lower Cr_{EQ}/Ni_{EQ} ratio in which the thermodynamically stable solidification mode is austenitic. The austenite dendrites are then found to continue growth across the weld junction into the undiluted regions of the high Cr_{EQ}/Ni_{EQ} ratio material. By providing austenite particles in this way, nucleation is rendered unnecessary and it is found that solidification to metastable austenite can be induced at cooling rates significantly lower than previously encountered. The results of these and other experiments in which the welding speed was changed during the experiment are interpreted to yield new information about the mechanisms of solidification and transformation in stainless steels during welding under conditions consistent with high cooling rates.

MST/1240

 Manuscript received 20 April 1990. *At the time the work was carried out the authors were in the Metals and Ceramics Division, Oak Ridge National Laboratory, Oak Ridge, Tennessee, USA. Dr Bhadeshia was there on leave from the Department of Materials Science and Metallurgy, University of Cambridge.*

List of symbols

C	concentration per unit volume
C_A	initial concentration of solute on side of junction where weld commences
C_B	initial concentration of solute on side of junction where weld finishes
C_i	weld pool composition after i steps
C_L	solute concentration in liquid phase
C_S^I	solute concentration in solid phase at solid/liquid interface
C_L^I	solute concentration in liquid phase at solid/liquid interface
C_S	solute concentration in solid phase
Cr_{EQ}	chromium equivalent
D	solute diffusivity at interface
D_L	solute diffusivity in liquid
D_S	solute diffusivity in solid
f_j	fractional volume of slab j in dilution model
k	partitioning coefficient, C_S/C_L
k_e	equilibrium partitioning coefficient
k_p	actual partitioning coefficient
Ni_{EQ}	nickel equivalent
v_D	diffusive velocity in Aziz solute trapping model
v_S	trapping velocity in Aziz solute trapping model
V_j	volume of slab j in dilution model
V_M	volume of largest slab in dilution model
V_{tot}	volume of weld pool in dilution model
w	weight fraction
Δy	thickness of slice in dilution model
λ	intersite jump distance across interface

Introduction

It has long been recognised that a significant problem in the production of fully austenitic stainless steel welds is their tendency to hot cracking and microfissuring. To minimise this tendency, the compositions of weld filler metals are generally modified to produce small amounts of δ-ferrite in the as-welded microstructure. Such compositional changes promote the formation of ferrite as the primary solidification phase. When austenitic stainless steel weld metal is exposed to elevated temperatures for extended periods of time, the ferrite can transform to a hard, brittle compound known as σ-phase.[1] This transformation has been shown to lead to low ductility creep ruptures when sufficiently high stresses are applied at elevated temperatures. Furthermore, ferrite can reduce the corrosion resistance.[2,3]

It would therefore be desirable to produce a fully austenitic weld microstructure that is resistant to cracking. Recent investigations have shown that rapid solidification of austenitic stainless steels may produce microstructures during solidification that are markedly different from those observed during conventional solidification.[4–7] Advances in rapid solidification processing and the use of high energy beam welding have emphasised the importance of cooling rate on the evolution of microstructure in stainless steels. During rapid solidification, the mode of solidification may change from ferritic to austenitic, even though the thermodynamically most stable phase might be ferrite. In addition, solute partitioning and resultant segregation patterns may be altered greatly. Whether these are desirable features of the process remains to be seen, since a fully austenitic solidification microstructure is generally thought to lead to hot cracking induced by the segregation of sulphur into the liquid. On the other hand, the rapid solidification associated with such a change in the mode of solidification might trap the sulphur, leading to a low, homogeneous concentration in the austenite, consequently avoiding the segregation problem.

With these and other issues, a clear understanding of the solidification and transformation sequences in stainless steels is necessary. The significant microstructural changes that have been observed in rapidly solidified and cooled austenitic stainless steels have been interpreted as resulting from either a change in the mode of solidification or a massive solid state transformation. It was the purpose of this experimental study to show conclusively that fully austenitic microstructures may be produced in certain steels as a result of a change in the mode of solidification. The possibility of a massive transformation occurring under some conditions is the subject of another ongoing study.

Experimental procedures

MATERIALS

The materials used in this investigation were from heats of three different commercial austenitic stainless steel filler

Table 1 Compositions of stainless steel samples, wt-%

AISI type	C	Si	Mn	P	S	Cr	Mo	Ni	Ti	Cr_{EQ}/Ni_{EQ}	Solidification type
308A	0·04	0·38	1·78	0·023	0·005	20·12	0·06	9·72	...	1·76	Ferritic
310B	0·03	0·42	0·90	0·013	0·005	25·62	0·15	19·18	...	1·29	Austenitic
316A	0·04	0·30	1·86	0·016	0·012	17·01	2·30	11·50	...	1·45	Ferritic
316B	0·03	0·45	2·22	0·042	0·018	19·25	2·34	12·73	0·39	1·51	Austenitic

metal alloys; their chemical compositions are listed in Table 1. The ferrite forming tendencies of the alloys are reflected in the ratio of their chromium and nickel equivalents, Cr_{EQ}/Ni_{EQ}, where[8]

$$Cr_{EQ} = [Cr] + [Mo] + [Si] + [Nb] \quad . \quad . \quad . \quad . \quad . \quad (1)$$

$$Ni_{EQ} = [Ni] + 30[C] + 0{\cdot}5[Mn] \quad . \quad . \quad . \quad . \quad . \quad (2)$$

and the concentrations are in wt-%. The alloys listed in Table 1 solidify under equilibrium conditions in either the primary austenitic or primary ferritic mode, as indicated. For convenience, the alloys are therefore referred to in this paper as either 'γ-alloys' or 'δ-alloys'.

WELDING

The filler metal alloys were prepared, as in an earlier investigation,[9] in the form of annealed sheets of 0·51 mm thickness. Some of the samples were later reduced in thickness to 0·25 mm by rolling in order to ensure full penetration during low heat input welding. The welds were made on thin sheet couples of stainless steels of two different compositions butted together (e.g. 310A/308B), the weld starting on a sheet of one composition and running into the other across the junction (Fig. 1). Laser beam welding was carried out using a pulsed Nd:YAG laser (Raytheon Model SS-550) capable of delivering an average power of 400 W. A 152 mm lens was used to focus the beam sharply onto the specimen surface. A pulse length of 1 ms and a pulse rate of 200 s^{-1} were used. During welding, an argon gas shield was used to protect the weld pool surface. In order to vary the heat input, and hence the cooling rate, welding speeds ranging from 0·85 to 32 mm s^{-1} were used. In some experiments the speed was varied, as discussed below. Unless otherwise stated, the laser power level was set to 190–200 W.

Gas tungsten arc (GTA) welds were made at speeds of 8·5 and 32 mm s^{-1}, using welding currents of about 25 and 47 A respectively, with an arc gap of 0·9 mm in each case. The tungsten electrode was 1·6 mm in diameter.

The scheme used to identify the samples is presented in Table 2; the last digit in each case represents the approximate welding speed in mm s^{-1}. Note that an R added to the end of the designation indicates that the weld was carried out in the reverse direction; thus, L1-2R denotes a laser weld started from the 308A side, and continued across the junction to the 310B side. Most of the laser welds were performed on samples 0·51 mm thick, but later experiments required a reduction in sample thickness to 0·25 mm, and those samples are identified by the letter T at the end of the designation.

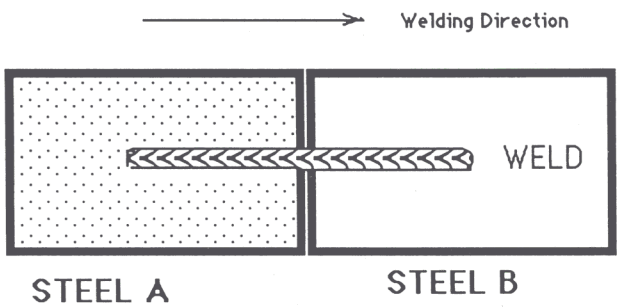

1 Schematic illustration of butt weld across dissimilar metal junction

MICROSTRUCTURAL CHARACTERISATION

Metallographic specimens were prepared for optical microscopy using conventional metallographic techniques and were etched using a solution of 3 vol.-% HNO_3 in water. Microanalysis measurements were made using a scanning electron microscope equipped with an energy dispersive X-ray detector. Compositions were determined after making corrections for atomic number, absorption, and fluorescence. Only the major constituents were analysed, namely iron, chromium, nickel, and molybdenum. The concentrations of these elements were normalised to 100 wt-%. Measurements were made on the undiluted alloys far from the dissimilar joint in order to provide a proper reference composition for the results.

The microanalysis experiments were carried out in order to establish the degree of dilution in the vicinity of the dissimilar stainless steel alloy junctions. The differences in composition of the individual phases present in the microstructure did not influence the measurements since the compositions were evaluated over a rastered area (~ 0·9 × 0·12 mm) that was very large compared with the scale of the microstructure (a few micrometres). Measurements were made along the welding direction at a fixed distance from the top surface of the weld. In addition, limited measurements were also made on the individual phases present in the microstructure. These were carried out in order to obtain information on the partitioning of chromium and nickel among the austenite and ferrite in the welds. In these experiments, a focused probe was used to achieve a spatial resolution of approximately 1 μm.

Table 2 Specimen identification scheme

Specimen	Weld technique	Speed, mm s^{-1}	Weld direction: From	Weld direction: To
L1-2	Laser	2·1	310B	308A
L1-2R	Laser	2·1	308A	310B
L1-2T	Laser	2·1	310B	308A
L1-9	Laser	8·5	310B	308A
L1-9T	Laser	8·5	310B	308A
L1-32	Laser	32	310B	308A
L1-32T	Laser	32	310B	308A
L2-1	Laser	0·85	310B	316B
L2-2	Laser	2·1	310B	316B
L2-2R	Laser	2·1	316B	310B
L2-9	Laser	8·5	310B	316B
L2-9R	Laser	8·5	316B	310B
L2-32	Laser	32	310B	316B
L3-2	Laser	2·1	310B	316A
L3-9	Laser	8·5	310B	316A
L3-32	Laser	32	310B	316A
G1-9	GTA	8·5	310B	316A
G1-21	GTA	21	310B	316A
G2-9	GTA	8·5	310B	316B
G2-21	GTA	21	310B	316B
G3-9	GTA	8·5	310B	308A
G3-21	GTA	21	310B	308A

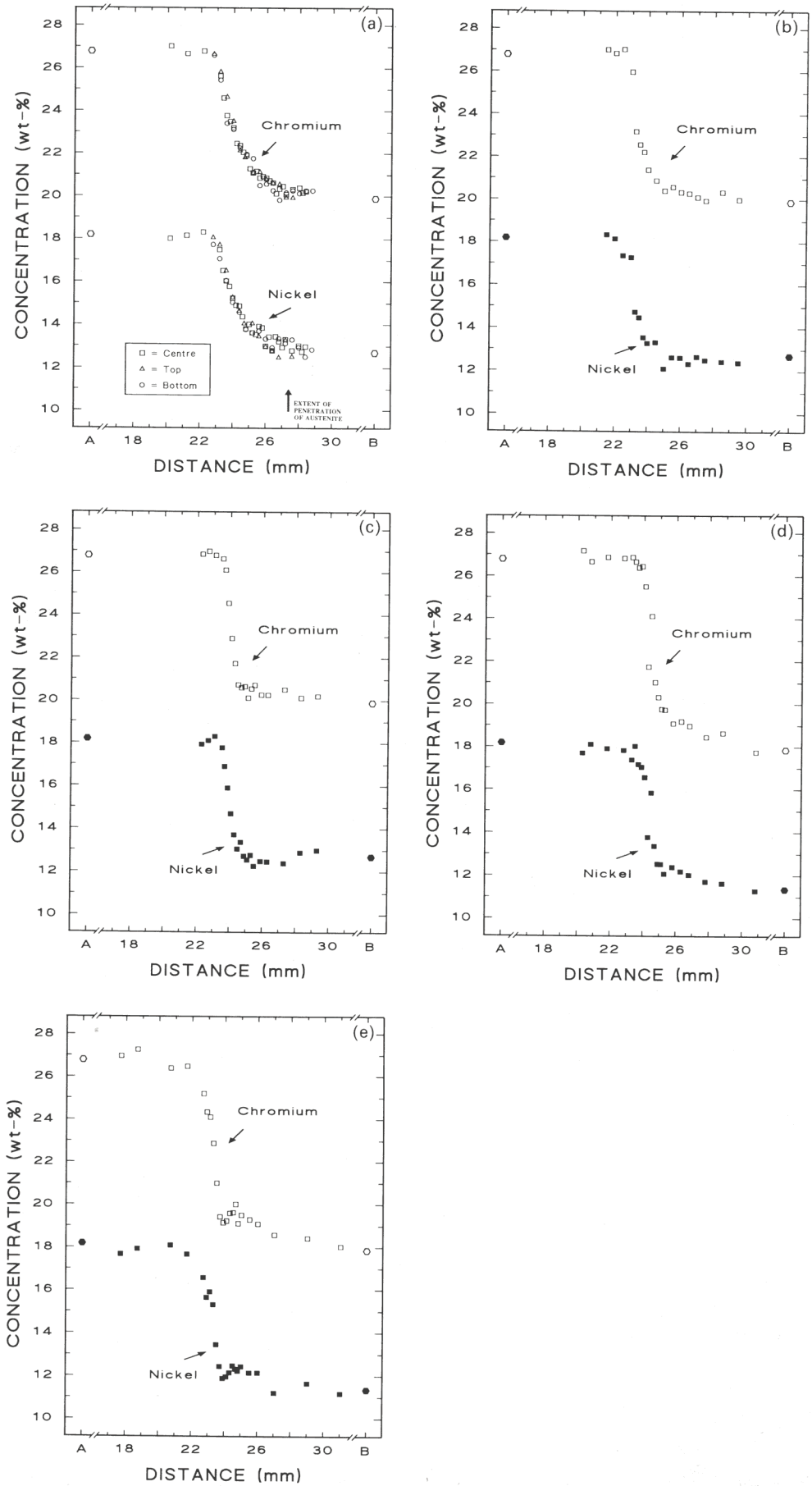

a L2-2; *b* L2-9; *c* L2-32; *d* G1-9; *e* G1-21

2 Microanalytical data illustrating extent of dilution associated with dissimilar metal joints, as function of distance normal to dissimilar metal junction; data in each case show changes in Cr and Ni concentrations, at top, middle, and bottom positions along depth direction, as discussed in text

Results

COMPOSITION MEASUREMENTS OF DILUTION AT DISSIMILAR STAINLESS STEEL ALLOY JUNCTIONS

Since the rate of dilution is expected to depend mostly on the weld pool size and shape (i.e. the welding conditions) rather than on the specific alloy chemistry of the dissimilar weld for the range of alloy combinations examined, samples typical of each of the welding conditions that were used were examined, and the results were taken to be representative of all the alloy combinations welded under similar conditions. The specific samples examined were 310B/316B laser welds made at 2·1, 8·5, and 32 mm s^{-1} (specimens L2-2, L2-9 and L2-32) and GTA welds of 310B/316A made at 8·5 and 21 mm s^{-1} (specimens G1-9 and G1-21).

The variation of composition with distance is plotted in Fig. 2. Also plotted are the alloy compositions for the initial (A) and final (B) alloys in the dissimilar welds. All the profiles show a rather steep initial change in composition followed by a more gradual decline to the composition of the undiluted alloy (alloy B). For the laser welds, the size of the region in which there is a transition in composition as the weld traverses from one alloy to the other was found to decrease as the welding speed was increased. For the GTA welds, the width of this transition zone did not change significantly in going from 9 to 21 mm s^{-1} travel speed. Although a direct comparison between GTA and laser weld transition zones is complicated by the fact that the dissimilar welds were made between two different pairs of alloys, in general the distance over which the composition gradually approaches the B composition is greater for the GTA welds. As shown in the next section, the width of the transition zone is directly proportional to the weld pool size. Therefore, the results indicate that the weld pool decreases in size as the welding speed increases, or when the process is changed from GTA to laser welding, as expected.

Composition profiles taken at different depths below the weld pool surface are shown in Fig. 2*a*. The results show that the weld pool profile does not change in shape at different depths. Furthermore, neither are the profiles shifted with respect to one another along the weld direction. As shown in the next section, where the dilution profiles are calculated, the shift (or lack of shift) is a direct consequence of the shape of the weld profile at the rear of the weld pool. The fact that there is no shift in composition profiles with increasing depth indicates that the rear profile of the weld pool must be quite steep. For full penetration welds such as that in specimen L2-2, such a steep weld pool shape can be expected.

DILUTION MODEL

For the dissimilar joint configuration examined in this study, in which the weld direction is normal to the metal junction, the authors are unaware of any calculations describing the degree of dilution as a function of distance along the weld. Therefore, the dilution process was modelled in an effort to understand and interpret the experimentally determined weld concentration profiles. The model considers the compositional changes produced by welding from alloy A to alloy B. It is assumed that the weld pool shape is constant across the alloy interface. Furthermore, it is assumed that the weld pool composition is uniform within the pool. This assumption seems reasonable in the light of the strong convection currents that exist in the weld pool, and also the smooth and continuous manner in which the composition was found to vary along the weld pool. Finally, compositional variations on a microscopic scale are ignored, and it is assumed that macrosegregation does not take place. Rather, the assumption is that, as the solidification front advances, the newly formed solid has the same composition as the liquid from which it is solidifying.

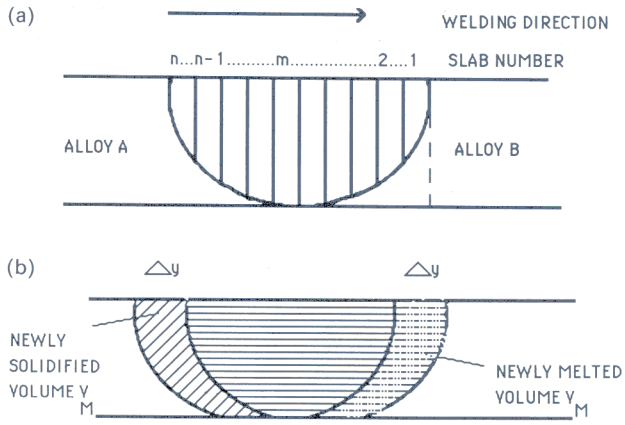

a initial weld pool divided into *n* slabs, just as it is about to cross dissimilar junction; *b* advance of weld pool one incremental step across dissimilar junction

3 Schematic diagram of dilution modelling procedure, illustrating how mixing of regions of different chemical composition occurs as pool advances across dissimilar metal junction

A schematic diagram of the advance of the weld pool, giving the quantities used to calculate dilution, is shown in Fig. 3. The dilution of the weld metal composition is modelled by the following progression. With the liquid pool of uniform composition, the solidification front at the rear of the pool is assumed to advance an increment Δy along the weld direction. The newly formed solid is of the same composition as the liquid. Then, the front of the pool is allowed to advance the same distance Δy, and thereby the original shape of the melt pool is recovered. In this last step, new material is melted. The liquid composition is adjusted to allow for the introduction of the newly melted material, and then the sequence is repeated. For simplicity, the weld pool is divided into n slabs, each of length Δy in the weld direction. In the present calculations, n was set equal to 10. Initially, a right cylindrical weld pool shape was assumed; other pool shapes were also considered and, as shown later, the results are not overly sensitive to the particular pool shape assumed.

Each slab has a volume V_j, $j = 1, \ldots, n$. The fractional volume of each slab is given by

$$f_j = V_j / V_{tot} \quad . \quad . \quad . \quad . \quad . \quad . \quad . \quad . \quad . \quad . \quad . \quad . \quad . \quad . \quad . \quad (3)$$

The slab with the maximum volume (corresponding to the maximum cross-sectional area) is the Mth slab ($1 \leqslant M \leqslant n$). It is easily shown that for each incremental step Δy along the weld direction, a volume V_M is solidified and a volume V_M of new material is melted. The compositions are then calculated as functions of the number of incremental advances of the weld pool, which corresponds directly to distance along the weld direction. The weld pool composition after i steps is denoted by C_i. Until the front of the weld pool crosses the interface between alloys A and B, the melt pool composition remains constant and is equal to the composition of alloy A. Therefore, for simplicity, the index i is set equal to zero when the front of the weld pool first crosses the joint. For the ith increment, where $1 \leqslant i \leqslant M$, the dilution effect is given by

$$C_i = (1 - f_M) C_{i-1} + (f_M - f_i) C_A + f_i C_B \quad . \quad . \quad . \quad . \quad (4)$$

and where $i \geqslant M$ the weld pool composition is given by

$$C_i = (1 - f_M) C_{i-1} + f_M C_B \quad . \quad . \quad . \quad . \quad . \quad . \quad . \quad . \quad (5)$$

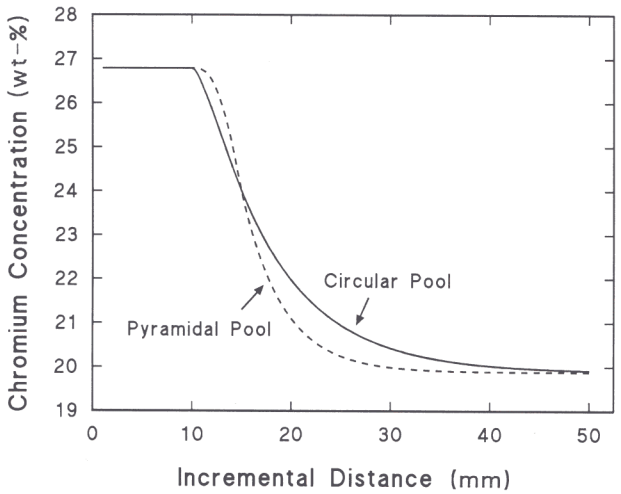

4 Calculated dilution profiles as function of model assumptions, for 310B/316B weld

These formulae simply reflect the fact that, as the weld pool advances an increment Δy, a fractional volume f_M is solidified, and the same fractional volume of new material melts and alters the weld pool composition. Although equations (3) and (4) are easily interpreted, they are not in a convenient form since the weld pool composition after i increments is given as a function of the weld pool composition after $i-1$ increments. The following equations eliminate this dependence: for $1 \leqslant i \leqslant M$

$$C_i = (1-f_M)^i C_A + C_A \sum_{k=0}^{i-1} [(1-f_M)^k (f_M - f_{i-k})] + C_B \sum_{k=0}^{i-1} [(1-f_M)^k f_{i-k}] \quad \ldots\ldots\ldots \quad (6)$$

and for $M \leqslant i$

$$C_i = (1-f_M)^i C_A + C_A \sum_{k=i-M+1}^{i-1} [(1-f_M)^k (f_M - f_{i-k})] + C_B \sum_{k=0}^{i-M} [(1-f_M)^k f_M] + C_B \sum_{k=i-M+1}^{i-1} [(1-f_M)^k f_{i-k}] \quad \ldots\ldots \quad (7)$$

The calculated variation in weld composition as a function of incremental distance is shown in Fig. 4. Compositions for alloys 310B and 316B used to calculate Fig. 4 are based on SEM microanalysis measurements since these compositions are later compared with experimentally determined composition profiles. The weld pool length is equal to $n \times \Delta y = 10\Delta y$ for these calculations. The calculations were made for a 310B/316B dissimilar weld. Curves are shown for two different assumed weld pool shapes: a right circular cylinder and a truncated pyramid. They show that the results are not sensitive to the assumed weld pool shape. The composition profiles indicate that the weld composition changes rather abruptly at first, and then gradually levels off at the composition of alloy B. These dilution profiles have the same shape as the experimentally determined composition profiles shown in Fig. 2.

Some general characteristics of the weld composition profiles can be given, based on the calculations. First, the weld pool composition changes immediately once the front edge of the weld pool crosses the dissimilar junction. Therefore, the weld composition is expected to begin to change one pool length away from the junction, on the A alloy side. Second, by the time the weld is solidifying at the location of the dissimilar junction, its composition has changed by about 75–85% of the difference between alloys A and B. At a distance of one pool length on the B side of the junction, the weld composition has changed by over 90% of the difference in alloy compositions. Finally, as can be seen in Fig. 3*b*, when the weld pool advances an incremental distance Δy the newly solidified volume lies along the rear of the weld pool. Since the composition of this newly solidified material is constant and equal to that of the liquid, it follows that the iso-concentration lines in the weld will follow the profile of the real surface of the weld. Thus, the variation in composition with depth will give a direct indication of the shape of the weld pool along this trailing edge.

DISSIMILAR ALLOY JOINTS

Alloy 310B is a stainless steel with such a low Cr_{EQ}/Ni_{EQ} ratio that, under all cooling conditions (ranging from equilibrium cooling to the highest cooling rates reported[9]), it solidifies as austenite. Furthermore, for the range of conditions considered in this work, some solute partitioning takes place during solidification, yielding a well defined and observable dendritic microstructure. The primary purpose of the experiments discussed below was to utilise steel 310B to induce some of the δ-alloys to solidify as austenite by eliminating the need to nucleate austenite. If the process of austenite growth from the liquid has a kinetic advantage over that of δ-ferrite growth, even though the austenite may be thermodynamically metastable, then austenite which forms when 310B is autogenously welded may continue to grow into a δ-alloy as the beam traverses from the 310B into the adjacent δ-alloy. By examining the continuity and penetration of austenite from the 310B side of the dissimilar metal joint into the δ-alloy, it should be possible to establish conclusively that δ-alloys are capable of solidifying as austenite, as long as the penetration of the austenite exceeds the distance over which dilution effects occur.

310B/308A

For the welding speeds used in the present experiments, it was previously established[9] that autogenous laser beam welding cannot induce steel 308A to solidify with austenite as the primary phase. At the lowest of the laser welding speeds (for specimen L1-2, Fig. 5*a*) used in the present work, some of the austenite dendrites were nevertheless found to continue to grow into the 308A, but the extent of penetration was not very large in comparison with the extent of dilution effects. Otherwise, a fairly blunt transition was observed at the junction between the two alloys in each of specimens L1-2, L1-9, and L1-32. On the other hand, a comparison of specimens L1-2 and L1-2R (Figs. 5*a* and 5*b*) shows that when the welding is carried out in the reverse sense (308A → 310B) there is no penetration of δ-ferrite into the 310B alloy. The fact that the transition in the reverse direction is very abrupt when compared with the diffuse and ragged transition for the forward weld (310B → 308A) indicates that the austenite has a kinetic advantage during the solidification of 308A.

Unexpectedly, all the results indicate that it becomes easier to propagate the austenite from the dissimilar metal junction into the 308A as the welding speed decreases or the heat input increases. The effect was confirmed for all metal combinations studied. This is intuitively unexpected because metastable austenite formation is more likely when the cooling rate increases (i.e. the heat input decreases). The reason for this becomes apparent when transverse sections of the welds are examined (Fig. 5*c*). Although dendrites of austenite can continue to grow across the dissimilar metal junction, as seen in the centre of the transverse section view in Fig. 5*c*, austenite growth becomes stifled by hard impingement with other dendrites that grow from the fusion zone boundary. In most cases these

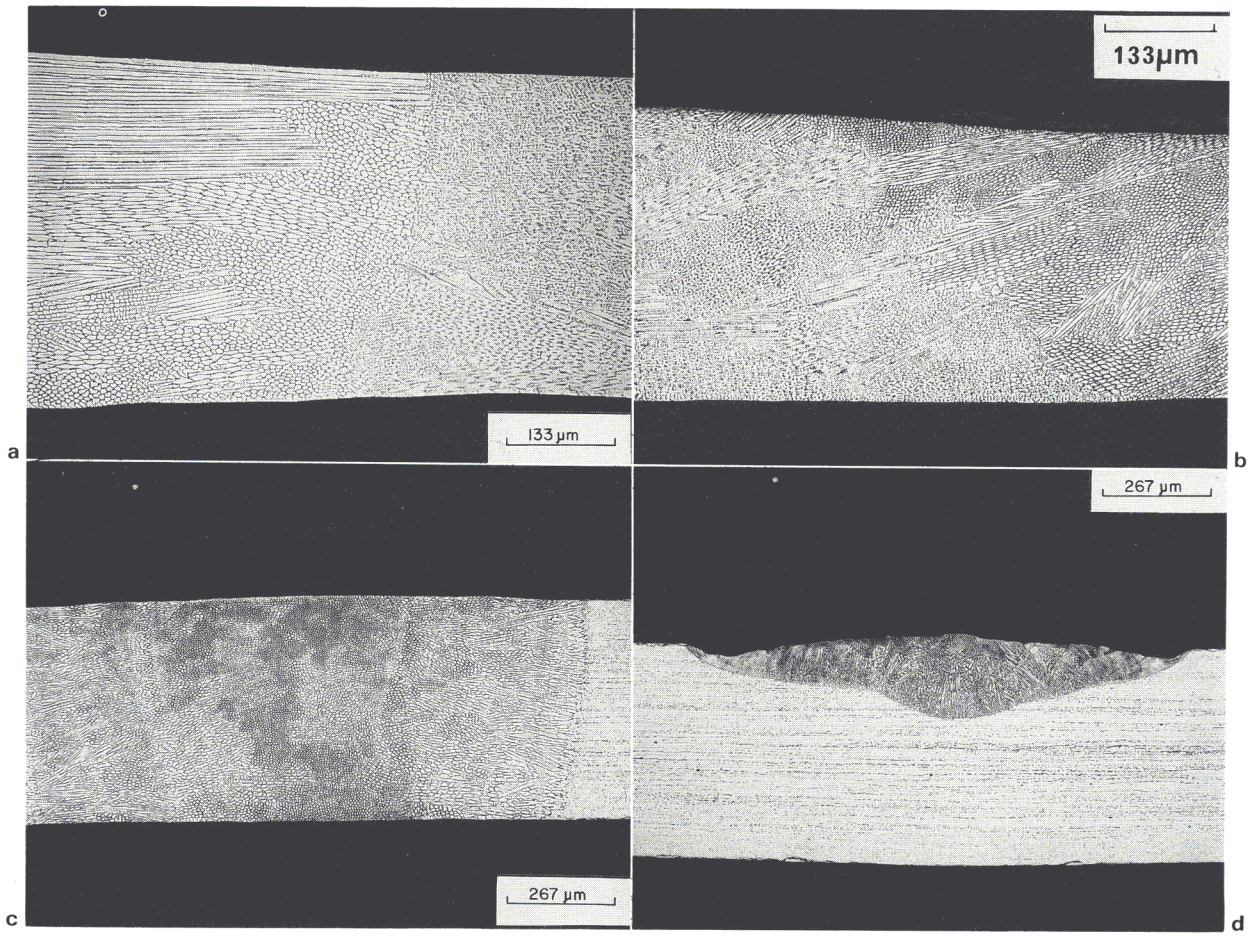

a penetration of austenite dendrites to 308A side of dissimilar metal junction in specimen L1-2; *b* specimen welded from 308A to 310B, L1-2R, showing relatively abrupt transition as junction is crossed; *c* transverse section of specimen L1-2, on 308A side of dissimilar metal junction, illustrating stifling of metastable austenite dendrites by those (δ-dendrites) growing directly from 308A sample fusion boundaries; *d* transverse section of specimen L1-32, showing enhanced stifling effect of partial penetration

5 Dissimilar metal joints between 308A and 310B alloys

impinging dendrites are of δ-ferrite, growing from the fusion boundary of the base δ-alloy. The effect is exaggerated as the weld pool size decreases, since the ratio of the fusion surface to the molten volume then increases. It is further exaggerated for partial penetration welds, since the bottom of the fusion surface provides an additional site for the growth of unwanted dendrites (Fig. 5*d*); the welds carried out at the highest speeds were all partial penetration welds.

An attempt was made to overcome the influence of impingement in partial penetration welds by reducing the thickness of the material used for the autogenous welds from 0·51 to 0·25 mm. The aim was to achieve full penetration during laser welding, thereby reducing the ratio of fusion surface to melt volume, and permitting the relatively unhindered growth of austenite dendrites across the dissimilar metal junction. These experiments confirmed rather spectacularly both the stifling hypothesis and the ability of the 308A δ-alloy to solidify as metastable austenite. Specimens L1-2T, L1-9T, and L1-32T, all of which were full penetration welds, solidified completely to austenite, with no discontinuity of microstructure across the 310B/308A junctions (Figs. 6*a* and 6*b*). Austenite penetrated the full length of the samples (25 mm).

Although the differences between the thick and thin samples have been interpreted in terms of impingement of the austenite dendrites with others growing directly from the fusion surface, another contribution to the differences observed as a function of speed may originate from the pool shape. As the welding speed increases, the pool shape changes from elliptical to a teardrop shape.[10] In the former case, there is a solidification front in the centre of the pool that is perpendicular to the weld direction (and weld centreline), and this promotes the extension of grains along the centreline. However, for teardrop shaped pools the solidification front is inclined at a large angle to the welding direction, in which configuration the growth of grains along the centreline should be more difficult. This is simply a contributory factor, since it cannot explain the thin sheet experiments in which, even at high welding speeds (where a teardrop pool shape is expected), austenite dendrites were found to cross the junction and penetrate extensively into the δ-alloy.

310B/316B

Judging from published data,[9] autogenous laser beam welds do not lead to primary austenite solidification in steel 316B, at least for welding speeds from 2 to 47 mm s^{-1}. None the less, examination of specimen L2-2 revealed that austenite dendrites had penetrated into relatively undiluted regions of alloy 316B. As in 310B/308A welds, higher speeds led to less penetration of austenite into the δ-alloy. No significant penetration of austenite could be seen in specimen L2-9 or L2-32; metallographic examination confirmed that this was due to the profuse growth of δ-dendrites from the fusion boundary within the 316B steel, growth which stifled the propagation of the austenite dendrites across the dissimilar metal junctions. The degree of austenite penetration for specimen L2-2 (Fig. 7*a*) was to

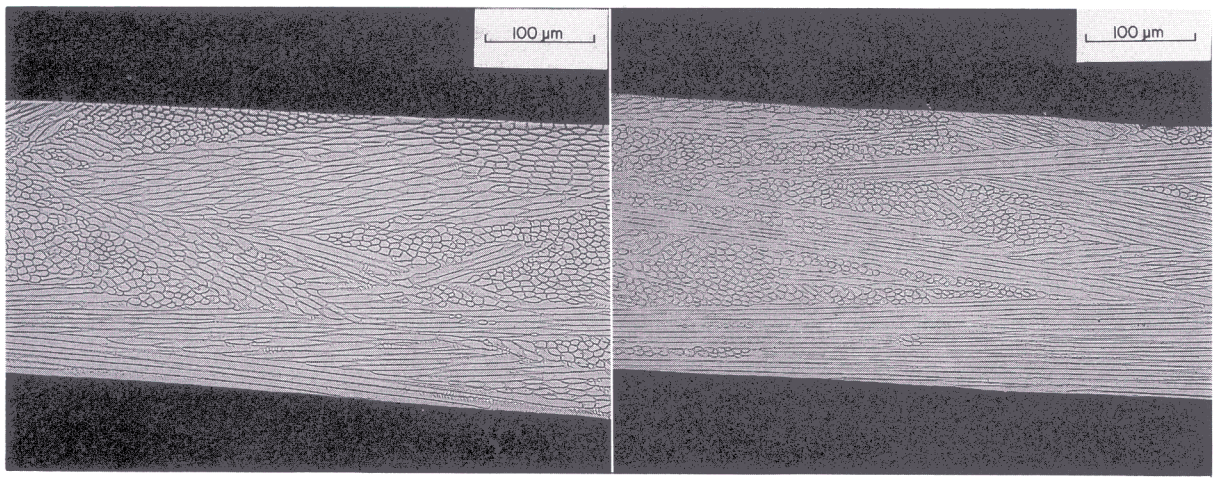

a micrograph of centre of dissimilar metal junction showing continuity of austenitic microstructure; *b* same sample photographed at 308A end, some 10 mm from junction, still showing austenitic microstructure

6 Complete penetration of metastable austenite dendrites into 308A side of specimen L1-2T, similar to L1-2 but welded using thinner sheet in order to achieve full penetration; entire weld is fully austenitic in all regions. Identical results were obtained for specimens L1-9T and L1-32T

the point shown in Fig. 2*a*. This penetration is larger than was observed for specimen L1-2. Examination of specimen L2-2R, in contrast, revealed a remarkably abrupt transition from ferritic to austenitic solidification (Fig. 7*b*); in fact, this transition was on the 316B side of the junction – before the junction was crossed. This, and the comparison with specimen L2-2, provides strong direct evidence that metastable austenitic solidification of 316B occurs because the austenite has a kinetic advantage over δ-ferrite during growth. Metastable δ-ferrite was not found to penetrate into steel 310B in specimen L2-2R, even though suitable austenite particles were available for propagation from

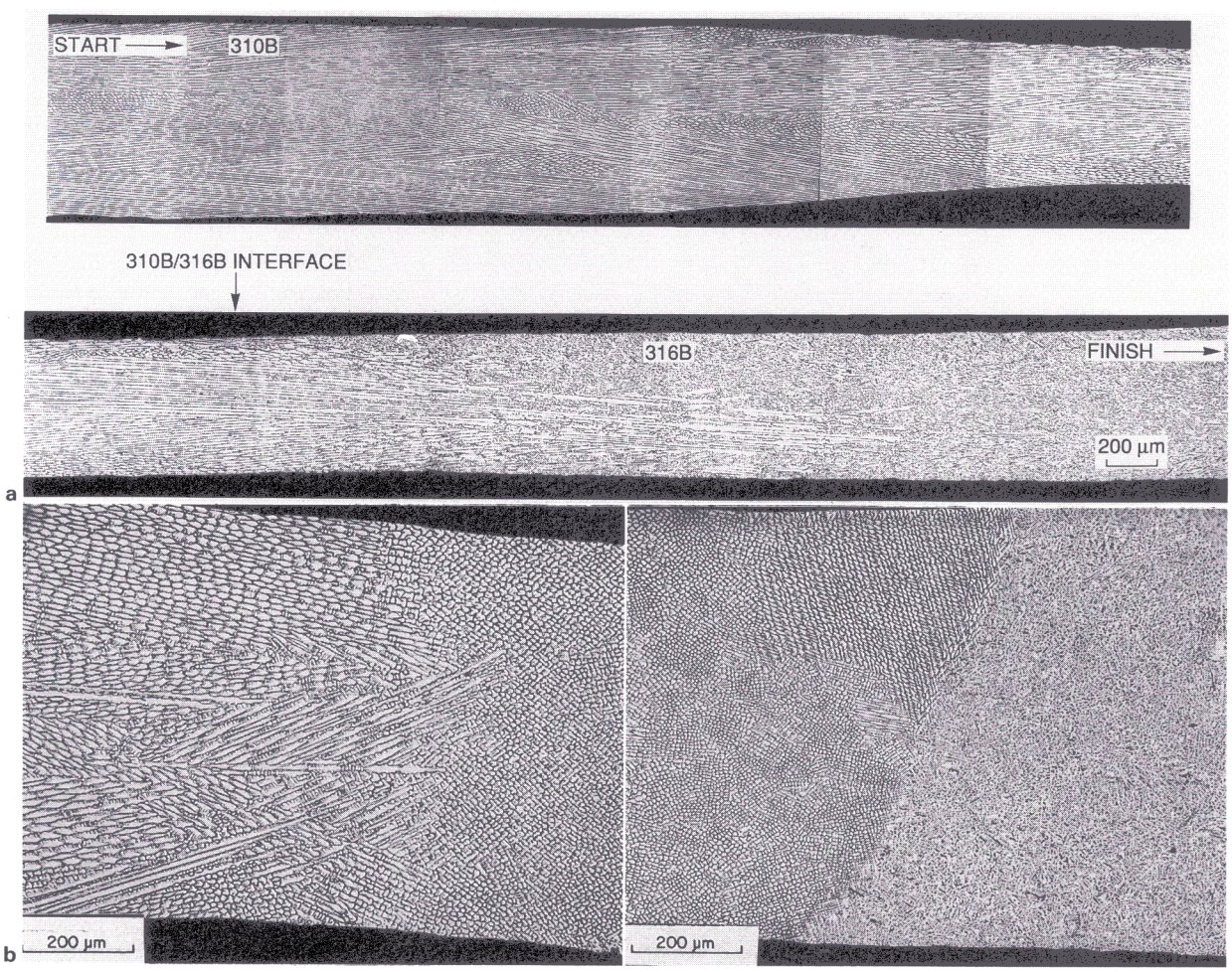

a montage illustrating penetration of metastable austenite dendrites into 316B side of dissimilar metal junction in specimen L2-2; *b* relatively abrupt microstructural transition when welding direction is reversed, specimen L2-2R; *c* similar abrupt transition in specimen L2-9R

7 Dissimilar metal joints between 310B and 316B alloys

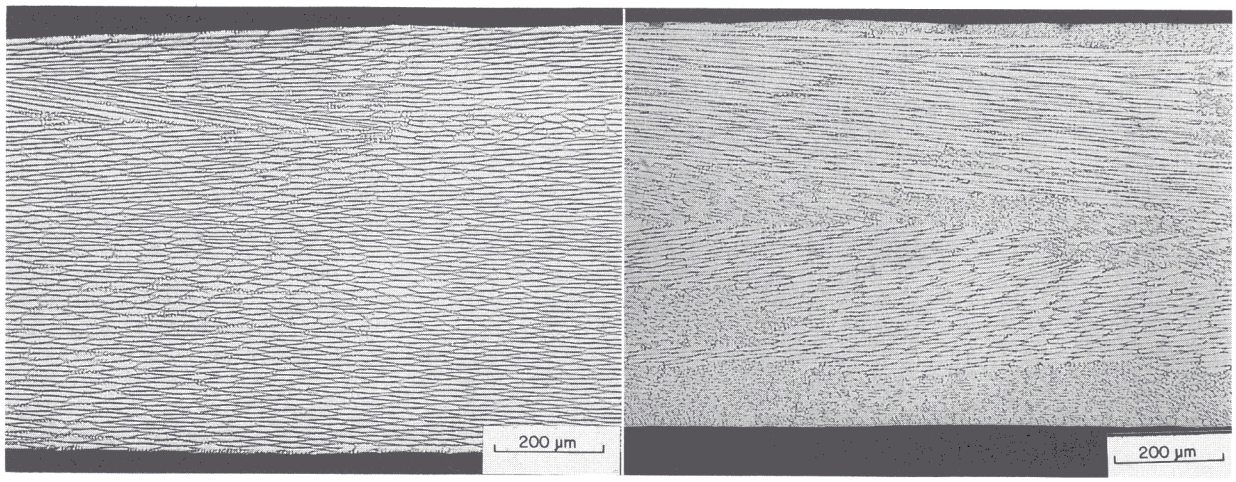

a specimen L3-2, approximately 1·9 mm on 310B side of junction; *b* specimen L3-2, some 5·9 mm from junction on 316A side, still showing austenite dendrites

8 Extensive penetration of austenite dendrites into 316A side of dissimilar metal junction

316B to 310B (identical to the results for the 308A/310B weld, L1-2R). In steel 310B, not only is the δ-ferrite thermodynamically not favoured, but the growth kinetics must be slower than for austenite. These results also explain why a ragged solidification transition region is obtained when welding from 310B towards 316B, whereas an abrupt transition occurs for the reverse direction of welding. In the former case, austenite dendrites can continue to grow until stifled by the δ-ferrite dendrites forming from the 316B substrate. Since such impingement will vary with circumstances (e.g. dendrite orientations) along the solidification front, the transition is irregular. For the reverse direction, though, the δ-ferrite solidification will be halted as soon as the pool composition changes sufficiently to promote austenite formation.

Similar results were observed for specimen L2-9R, which also revealed an abrupt transition, from the region which solidified with δ-ferrite as the primary phase to that which solidified to primary austenite (Fig. 7*c*). Such a region provides a unique opportunity to observe differences in $L \rightarrow \delta$ and $L \rightarrow \gamma$ solute partitioning behaviour for the same overall composition, since the average solute concentration in the close proximity of either side of the transition is similar.

Using scanning electron microscopy, microanalysis of the dendritic and interdendritic regions on either side of the transition surface of specimen L2-9R was performed. The interdendritic regions represent the microstructure that evolves from the final liquid to solidify, and a comparison of their compositions with that of the dendrite cores should reveal the nature of partitioning during the solidification process. For comparison purposes, similar data were collected from undiluted regions on either side of the junction, far from the transition zone. The results are presented in Table 3, where the data have been interpreted in terms of a partition ratio $k = C_S/C_L$, where C_S and C_L are the concentrations in the solid and liquid phases at the solidification temperature. For the purposes of the present work, C_S is assumed to be given by the dendrite core composition (the first solid to form), and C_L by the average composition of the solidifying alloy, since the composition of the liquid which is in equilibrium with the first solid to form is clearly the average alloy composition. The microanalysis experiments are only estimates of the true partition coefficients because the spatial resolution is too coarse to yield the interface compositions, and because the experiments deal with continuous cooling rather than isothermal transformation. There might also be stereological errors in identifying features such as dendrite cores from two dimensional metallographic sections.

The data are nevertheless useful since the main purpose here is to determine whether the partition coefficients depend on the solidification mode for the same average composition. This is clearly verified by the data, since the k values measured near the transition surface are found to be significantly different, both in their absolute values and in the sign of their difference with unity, for the δ-ferrite and austenite solidification modes. The partitioning trends for the regions near the transition surface are consistent with the measurements made far from the interface.

310B/316A

Steel 316A (another δ-alloy) has a lower Cr_{EQ}/Ni_{EQ} ratio than does steel 316B, and is consequently easier to induce into the austenitic solidification mode. During autogenous laser welding at the same power level as in the present work, 316A has been reported[9] to solidify as primary austenite at welding speeds of 8·5 mm s^{-1} and faster, but for a welding speed of 2·1 mm s^{-1} δ-ferrite solidification

Table 3 Microanalysis data obtained at positions where transition occurs in solidification mode, in specimens L2-2R and L2-9R; partition ratios *k* are ratios of concentration in dendrite core to average composition in locality; average composition is determined from rastered area much greater than microstructural scale

Transition location	Solidification mode	Dendrite core composition, wt-%		Average composition, wt-%		Partition ratios	
		Ni	Cr	Ni	Cr	k_{Ni}	k_{Cr}
L2-2R, 316 side	δ	14·3	24·4	15·4	23·3	0·93	1·05
L2-9R, 316 side	δ	13·0	27·6	16·3	24·6	0·80	1·12
L2-2R, 310 side	γ	15·7	22·1	15·4	23·2	1·02	0·95
L2-9R, 310 side	γ	16·1	23·7	16·5	24·5	0·98	0·97

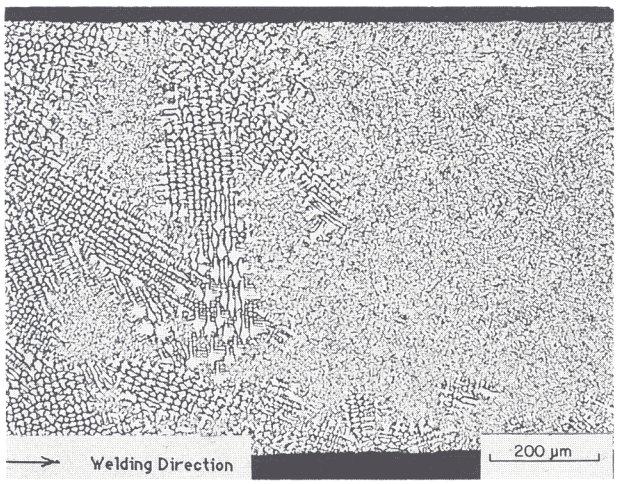

9 Austenite dendrites in GTA weld G1-9, about 6·8 mm on 316A side of dissimilar metal junction

occurs. Examination of specimens L3-2, L3-9, and L3-32 revealed extensive penetration of austenite dendrites. In fact, austenite dendrites often extended to the limits of the specimen dimensions, from 310B to 316A, far beyond the extent of any dilution effects (Fig. 8). Specimens L3-9 and L3-32 solidified as fully austenitic samples throughout, whereas in specimen L3-2 mixtures of primary austenite dendrites and regions which had solidified as primary ferrite could be seen far from the dissimilar metal junction (Fig. 8*b*). Thus, the 310B/316A combination laser welds behave unlike the other combinations, in that the higher speed welds show all austenite, while the lower speed welds show a mixed microstructure. In the other cases austenite was found in the higher heat input (low speed) welds. This is because of the greater stability of the austenite in 316A (Table 1), so that even in autogenous welds (Table 4) it tends to solidify to austenite. In the other cases (discussed below), the penetration of austenite across the junctions is stifled, for high speed welds, by δ-ferrite dendrites growing from the fusion surface.

These results were confirmed by examination of specimens G1-9 and G1-21, where the austenite was found to penetrate to distances far greater than the measured extent of significant dilution effects, which are $\sim 2{\cdot}25$ and $\sim 2{\cdot}75$ mm from the interface for G1-9 and G1-21, respectively, as measured and shown in Fig. 2. In specimen G1-9, primary austenite dendrites were found over 9 mm beyond the junction – to the full extent of the 316A side of the sample (Fig. 9). In specimen G1-21, the main austenite/dendrite front reached a distance of 6·9 mm from the 316A/310B junction, although some austenite dendrites could be observed at far greater distances.

The results of all the dissimilar metal joint experiments are summarised and compared against published data[9] on equivalent autogenous welds in Table 4.

VARIABLE SPEED EXPERIMENTS

Having established that some of the stainless steels could be solidified to metastable austenite when welded at high cooling rates, it was decided to address an additional microstructural issue which had previously been noted.[9] At moderately high welding speeds, metastable austenite dendrites are, in general, easily revealed by using optical microscopy on samples in which the chemical segregation patterns respond to etching, or in which small quantities of interdendritic ferrite might form in the heavily enriched interdendritic regions. However, as the welding speed is increased further, small patches of rather 'structureless' austenitic areas appear within the obviously dendritic austenite surroundings, and at even higher speeds these structureless regions tend to dominate the microstructure.[9] These regions have been found to show little response even to relatively heavy etching. In the light of such behaviour, it could reasonably be concluded that, as the degree of solute partitioning decreases with increasing speed during solidification, the coring effect diminishes in magnitude until it becomes difficult to reveal the dendritic shape of the austenite by etching, thereby giving an apparently structureless austenite. To test this concept, a variable speed experiment was designed in which alloy 316A was autogenously laser welded. The welding speed was initially held constant at $42{\cdot}3\ \text{mm s}^{-1}$, but after a certain length of weld had been produced the speed was decreased steadily to zero and the welding process discontinued.

The aim of the experiment was to observe a structureless region (with little or no obvious coring) change continuously into a cored austenite dendrite. The results are illustrated in Fig. 10, from which it is apparent that the structureless region is continuous with the dendrite. It was found that the degree of coring appeared to increase as the speed decreased. Microanalytical data collected using energy dispersive X-ray analysis on a scanning electron microscope on the areas in Fig. 10 confirmed that, as expected, the degree of partitioning is larger in the obviously dendritic metastable austenite than in the rather featureless austenite which develops at higher welding speeds.

Discussion

It is well established that many stainless steels, when autogenously welded using power beam techniques, can be

Table 4 Summary of published data (autogenous laser welds[9]) and present results on mode of solidification in austenitic stainless steels which are laser welded; γ and δ denote primary austenitic and primary ferritic solidification, respectively. While most dissimilar metal laser welds were fabricated using sheet of thickness 0·51 mm, in some cases welds were repeated using sheet of half that thickness (denoted by subscript T)

Speed, mm s^{-1}	Process	Autogenous 308A	Dissimilar 308A*	Autogenous 316B	Dissimilar 316B*	Autogenous 316A	Dissimilar 316A*
0·85	Laser	...	...	...	δ	...	...
2·1	Laser	δ	γ/γ_T	δ	γ	δ	γ
2·1	GTA	δ	δ	δ	δ	δ	γ
8·5	Laser	δ	γ/γ_T	δ	δ	γ	γ
8·5	GTA	δ	δ	δ	δ	δ	γ
21·1	Laser	δ	δ/γ_T	δ	δ	γ	γ

*Welds initiated in alloy 310B.

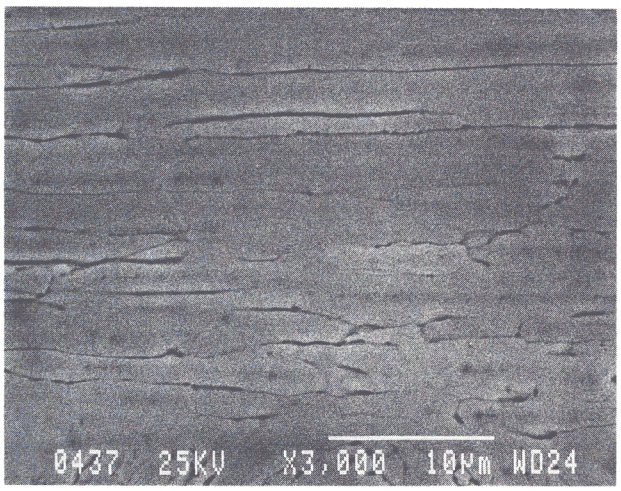

10 Sample of autogenously laser welded 316A stainless steel, using variable welding speed, showing continuous transition from cored metastable austenite dendritic microstructure to relatively featureless austenitic microstructure (SEM)

induced to solidify to metastable austenite rather than the thermodynamically stable δ-ferrite. The results presented here reveal a number of new features of this behaviour. All studies of the metastable solidification of stainless steels have so far focused on the relative growth rates of austenite and δ-ferrite in δ-alloys. However, metastable austenite formation first requires the nucleation of austenite, since the base material at the fusion boundary is expected to be ferritic. By completely removing the need to nucleate austenite, it has been demonstrated here that the steels can be induced into the austenitic solidification mode at cooling rates significantly lower than previously reported. This constitutes direct evidence that any kinetic model attempting to predict the transition from ferritic to austenitic solidification must also address the problem of nucleating the austenite. The kinetics of δ-ferrite growth, which would involve the epitaxial growth of grains from the base material at the fusion surface, need to be compared with the nucleation and growth kinetics of austenite. Given that – even for the highest of cooling rates considered – the melts are unlikely to be undercooled by more than a few degrees, the models must predict a kinetic advantage for austenite at temperatures not far from the equilibrium melting temperature of the alloy concerned.

The present work shows conclusively that the alloys studied are capable of austenitic solidification. For most of the cooling rates used, the solidification is not found to be partitionless since segregation patterns are observed on etching to reveal the dendrite form. Since the microstructures seen for the austenitic dissimilar metal joints are identical to those reported for the austenitic autogenous welds,[9] the experiments strongly support the conclusion that the microstructures evolve as a consequence of austenitic solidification. The featureless microstructures observed at high cooling rates thus arise from nearly partitionless austenitic solidification, consistent with the difficulty in metallographically revealing the segregation patterns. This hypothesis has received further support from the results of the variable speed experiments. It is expected from theoretical predictions[11–13] that the partitioning of solute becomes more difficult as the solid/liquid interface moves at higher velocities, and this should lead to a reduction in the segregation patterns. This would again be consistent with the present observations, and the feasibility of this hypothesis is examined next, using solute trapping theory.

SOLUTE TRAPPING

The phenomenon of solute trapping has been known for as long as martensitic transformations have been recognised. Its formal definition is that a species is said to be trapped when its chemical potential increases on transfer across the interface.[11] Aziz[12,13] has derived a model for solute trapping which is physically simple to understand: if the velocity v_S of the interface is larger than the diffusive velocity v_D of the solute, then solute trapping becomes prominent and the compositions of the phases at the interface will show deviations from equilibrium.

In the present context, solute trapping is important because as the welding speed is increased there will be a tendency to partitionless solidification. Initially, solidification to metastable austenite is not expected to be partitionless, and this is consistent with the fact that the etching reveals the dendritic forms of the austenite. The segregation during solidification is also found to lead to the formation of small amounts of intercellular ferrite on occasions. As partitionless solidification is approached, the dendritic form will not be revealed by etching, and this may be the explanation for the observation of an apparently different kind of austenitic microstructure at high welding speeds, a microstructure sometimes attributed to a massive transformation from δ-ferrite.

Let us define the partitioning coefficient $k_p = C_S^I/C_L^I$, where C_S^I and C_L^I are the concentrations in the solid and liquid phases at the interface, respectively. The Aziz model predicts that, for continuous growth,

$$v_S = v_D\left(\frac{k_p - k_e}{1 - k_p}\right) \quad \ldots\ldots\ldots\ldots \quad (8)$$

where k_e is the equilibrium partitioning coefficient, and the diffusive velocity is given by

$$v_D = D/\lambda \quad \ldots\ldots\ldots\ldots \quad (9)$$

Here D is the solute diffusivity in the interface and λ is the jump distance across the transformation interface (the 'thickness' of the interface), assumed to be $\sim 0{\cdot}25$ nm. The diffusivity should be somewhere between those of the solid (D_S) and liquid (D_L) phases. It has been suggested[14] that averaging these diffusivities should take account of the height of the respective activation barriers, so that

$$D = (D_S D_L)^{1/2} \quad \ldots\ldots\ldots\ldots \quad (10)$$

Diffusion coefficients for liquid metals are not known precisely, but Friedberg *et al.*[15] state that they should be around 10^{-9} m^2 s^{-1}. This turns out, as might be expected, to be almost equal to the value of the grain boundary diffusivity of nickel in austenitic steel[16] at the solidification temperature. Hence the following values[17–20] were used to calculate the results presented in Table 5, with the assumption that diffusivity in the liquid is given by that in

Table 5 Equilibrium or metastable equilibrium partition coefficients for alloy 316A, calculated with concentrations expressed in weight fractions, so that $k_e^{Ni} = w_{Ni}^S/w_{Ni}^L$; calculations carried out for 20 K intervals

T, K	γ-solidification		δ-solidification	
	k_e^{Ni}	k_e^{Cr}	k_e^{Ni}	k_e^{Cr}
1695	1·06	0·88	0·78	1·05
1675	1·09	0·88	0·77	1·05
1655	...	...	0·77	1·05
1635	...	...	0·77	1·03
1615	...	...	0·78	1·01

a grain boundary:

$$\lambda D^{Ni}_{\gamma-boundary} \approx \lambda D_L = 3{\cdot}7 \times 10^{-15} \exp\left(-\frac{131\,796}{RT}\right) m^3\,s^{-1} \quad (11)$$

$$D^{Ni}_{\gamma} = 8{\cdot}8 \times 10^{-7} \exp\left(-\frac{251\,040}{RT}\right) m^2\,s^{-1} \quad (12)$$

$$D^{Cr}_{\gamma} = 1{\cdot}3 \times 10^{-5} \exp\left(-\frac{264\,010}{RT}\right) m^2\,s^{-1} \quad (13)$$

$$D^{Ni}_{\delta} = 7{\cdot}0 \times 10^{-7} \exp\left(-\frac{224\,262}{RT}\right) m^2\,s^{-1} \quad (14)$$

$$D^{Cr}_{\delta} = 6{\cdot}0 \times 10^{-6} \exp\left(-\frac{212\,129}{RT}\right) m^2\,s^{-1} \quad (15)$$

where R is the universal gas constant (J mol^{-1} K^{-1}).

The solidification velocity v_S is related to the welding speed. However, this relationship depends on the solidification front orientation (i.e. the location on the weld pool interface) and the orientation of the growing dendrite.[21] The solidification velocity lies between 0 and $3^{1/2}$ times the welding speed. For the present evaluation, the solidification velocity is taken as equal to the welding speed.

EQUILIBRIUM PARTITIONING COEFFICIENTS

The solute trapping analysis requires a knowledge of the equilibrium or metastable equilibrium partitioning coefficients for the L→γ and L→δ transformations in the solidification temperature range, as a function of alloy composition. The data have to be available for these two-phase combinations (even though more than two phases can exist during thermodynamic equilibrium) and in domains of the phase diagram where the phase concerned may be metastable. Thermodynamic calculations of the partition coefficients were carried out using the THERMO-CALC system, for the alloys of interest in the present work, and taking account of the Fe, C, Si, Mn, Cr, Mo, Ni, and Ti concentrations. The results are summarised in Table 5.

Table 6 Change in solute trapping for steel 316A as function of v_S

T, K	v_S, mm s^{-1}	k_p^{Cr}	k_p^{Ni}	Mode
1695	0·85	1·054	0·784	δ
1695	2·1	1·053	0·791	δ
1695	8·5	1·051	0·817	δ
1695	31·7	1·046	0·875	δ
1695	42·3	1·044	0·890	δ
1675	0·85	1·054	0·779	δ
1675	2·1	1·054	0·786	δ
1675	8·5	1·052	0·817	δ
1675	31·7	1·046	0·880	δ
1675	42·3	1·043	0·896	δ
1655	0·85	1·048	0·777	δ
1655	2·1	1·047	0·785	δ
1655	8·5	1·045	0·820	δ
1655	31·7	1·039	0·887	δ
1655	42·3	1·037	0·903	δ
1635	0·85	1·030	0·779	δ
1635	2·1	1·030	0·789	δ
1635	8·5	1·029	0·827	δ
1635	31·7	1·024	0·896	δ
1635	42·3	1·023	0·912	δ
1615	0·85	1·006	0·789	δ
1615	2·1	1·006	0·796	δ
1615	8·5	1·006	0·838	δ
1615	31·7	1·005	0·907	δ
1615	42·3	1·005	0·923	δ
1695	0·85	0·879	1·061	γ
1695	2·1	0·883	1·057	γ
1695	8·5	0·897	1·044	γ
1695	31·7	0·928	1·023	γ
1695	42·3	0·937	1·019	γ
1675	0·85	0·879	1·090	γ
1675	2·1	0·883	1·083	γ
1675	8·5	0·899	1·061	γ
1675	31·7	0·933	1·031	γ
1675	42·3	0·942	1·025	γ

APPLICATION OF SOLUTE TRAPPING THEORY

Some representative calculations of the partitioning coefficients as functions of growth velocity are presented in Table 6; the calculations utilise the equilibrium partition coefficients given in Table 5 and cover the theoretical liquidus to solidus temperature range for each solidification mode (with the restriction that data were available for 20 K intervals). The alloys are unlikely to be undercooled to more than a few degrees below the equilibrium solidus for the welding conditions used here. Inspection of the results shows that, with solidification to δ-ferrite, partitionless growth is unlikely even at the highest welding speeds used, significant amounts of nickel being displaced into the liquid phase during solidification. However, austenitic solidification approaches partitionless growth more closely at the highest welding speeds, both the nickel and chromium partitioning coefficients tending to within about $\pm$0·05 of unity. This can be attributed largely to the fact that the overall degree of equilibrium partitioning for austenite (Table 5) is smaller than for δ-ferrite, and because the diffusivity of solute in the ferrite is generally higher (this effect comes in via the calculation of the averaged diffusivity used in the trapping model).

Conclusions

Consistent with published data, it has been demonstrated experimentally that alloys which, on thermodynamic grounds, should solidify to δ-ferrite as the primary phase can be induced by rapid cooling to solidify as metastable austenite. In addition, it has been established experimentally that, if the barrier to the nucleation of austenite can be eliminated, then solidification to metastable austenite can occur at relatively low solidification rates. The experimental results suggest that for all the steels studied, the metastable austenite growth rate at the solidification temperature is faster than that of δ-ferrite, and that this is the key reason why high chromium equivalent stainless steels nevertheless may solidify to austenite. It appears that the featureless solidification microstructures often obtained at high solidification rates are a consequence of solute trapping, which results in a more homogeneous solid, rather than of any fundamental change in the sequence of transformation from the liquid phase.

Acknowledgments

The authors are especially grateful to Professor G. B. Olson of Northwestern University for the thermodynamic calculations, to Mr R. W. Reed for considerable help with the experimental work, and to Dr T. Zacharia for valuable discussions. They would also like to thank Dr J. R. Kaiser and Dr C. G. McKamey for reviewing the manuscript. The research was sponsored by the Division of Materials Sciences, US Department of Energy, under contract No. DE-AC05-84OR21400 with Martin Marietta Energy Systems, Inc.

References

1. M. O. MALONE: *Weld. J.*, 1967, **46**, 241s–253s.
2. J. HONEYCOMBE and T. G. GOOCH: *Met. Constr.*, 1972, **4**, 456–460.
3. R. VISWANATHAN, J. I. NURMINEN, and R. G. ASPDEN: *Weld. J.*, 1979, **58**, 118s–126s.
4. S. A. DAVID and J. M. VITEK: in 'Lasers in metallurgy', (ed. K. Mukherjee and J. Mazumder), 247; 1982, Warrendale, PA, The Metallurgical Society of AIME.
5. J. M. VITEK, A. DASGUPTA, and S. A. DAVID: *Metall. Trans.*, 1983, **14A**, 1833–1841.
6. S. KATAYAMA and A. MATSUNAWA: in Proc. ICALEO 84, 1984, 44, L1.A, 60–67.
7. J. W. ELMER: Doctor of Science in Metallurgy Thesis, Massachusetts Institute of Technology, 1988.
8. A. L. SHAEFFLER: *Met. Prog.*, 1949, **56**, 680–688.
9. S. A. DAVID, J. VITEK, and T. L. HEBBLE: *Weld. J.*, 1987, **66**, 289s–300s.
10. K. E. EASTERLING: 'Introduction to the physical metallurgy of welding', 53; 1983, London, Butterworths.
11. J. C. BAKER and J. W. CAHN: 'Solidification', 23–58; 1970, Metals Park, OH, American Society for Metals.
12. M. J. AZIZ: *J. Appl. Phys.*, 1982, **53**, 1158–1168.
13. M. J. AZIZ: *Appl. Phys. Lett.*, 1983, **43**, 552–554.
14. M. J. AZIZ: Harvard University, personal communication to H. K. D. H. Bhadeshia, 1989.
15. J. FRIEDBERG, L.-E. TÖRNDAHL, and M. HILLERT: *Jernkontorets Ann.*, 1969, **153**, 263–276.
16. R. A. PERKINS: *Metall. Trans.*, 1973, **4**, 1665–1669.
17. G. F. HANCOCK and G. M. LEAK: *Met. Sci. J.*, 1967, **1**, 33–36.
18. R. A. PERKINS, J. R. PADGETT, and N. K. TUNALI: *Metall. Trans.*, 1973, **4**, 2535–2540.
19. A. F. SMITH: *Met. Sci.*, 1975, **9**, 375–378.
20. A. F. SMITH: *Met. Sci.*, 1976, **10**, 418–423.
21. M. RAPPAZ, S. A. DAVID, J. M. VITEK, and L. A. BOATNER: *Metall. Trans.*, 1989, **20A**, 1125–1138.